ADVANCED FUNCTIONAL MATERIALS
www.afm-journal.de

Rational Fine-Tuning of MOF Pore Metrics: Enhanced SO_2 Capture and Sensing with Optimal Multi-Site Interactions

Shanghua Xing, Abdulrahman Mohabbat, István Boldog, Jens Möllmer, Marcus Lange, Yulyan Haiduk, Tobias Heinen, Vladimir Pankov, Oliver Weingart, and Christoph Janiak**

Selective capture of sulfur dioxide (SO_2), important in the context of environmental protection, is reachable by specially tailored porous materials endowed with physisorptive complementarity. Metal–organic frameworks (MOFs) can potentially be leading materials for physisorptive SO_2 capture due to their excellent tailorability. Here, a series of highly stable DMOFs, $[Ni_2L_2(DABCO)]$, where L = 1,4-benzenedicarboxylate (BDC), 1,4-naphthalenedicarboxylate (NDC), 2,6-naphthalenedicarboxylate (2,6-NDC), 9,10-anthracendicarboxylate (ADC), and 1,4-diazabicyclo[2,2,2]octane (DABCO) aiming at optimal SO_2 physisorption characteristics, is reported. The extension of the aromatic core by conjugated benzene rings allows to reach an optimal pore diameter at 4–5 Å in the case of the DMOF-ADC, maximizing the multi-site MOF···SO_2 interactions, which improve the SO_2 binding at low concentrations, as revealed by density-functional theory (DFT) calculations. The improved SO_2 separation performance of DMOF-ADC is demonstrated by single SO_2 and SO_2/CO_2-mixed-component adsorption (a SO_2/CO_2 selectivity >100 is reached at 0.01 bar, which is significantly better than the value for the benchmark DUT-8 material) and dynamic breakthrough experiment. The use as a chemiresistive sensor for SO_2 sensing is demonstrated for the best performing DMOF-ADC at low concentrations (doubled resistive response at 100 ppm and $T < 120$ °C).

1. Introduction

Anthropogenic sulfur dioxide (SO_2), primarily emitted as flue gases of fossil fuel combustion, is an atmospheric contaminant of primary concern.[1] The well-established desulfurization technologies such as limestone scrubbing or amine-based adsorption can remove a large fraction (90–95%) of SO_2 from flue gases.[2] However, these energy-intensive technologies leave residual SO_2 amounts.[3] The presence of SO_2 in flue gases also interferes with the CO_2 scrubbing and the incomplete removal of the former causes significant environmental issues, including long-term health hazards.[4] The maximally complete and more energy-effective removal of SO_2 from flue gases is an important task calling for further optimization.

Solid adsorbent-based gas separation through physisorption is a promising and arguably the most energy-efficient technology for deep desulfurization. If low-energy van der Waals (vdW) interactions are responsible for the adsorption, then this allows for an energetically economic regeneration of the adsorbent.[5] Various metal–organic frameworks (MOFs) as designable adsorbents have been developed for CO_2, CH_4 and hydrocarbon adsorption/separation. Their development was inspired by rationalizable reticular synthesis, which includes targeting desired pore sizes and the nature of pore surface due to the tailorability of the organic constituents.[6–8] However, only a handful of MOFs have been tried in the role of SO_2 adsorbents because of the highly

S. Xing
Academy of Food Interdisciplinary Science
School of Food Science and Technology
Dalian Polytechnic University
Qinggongyuan1, Ganjingzi District, Dalian, Liaoning 116034, China
E-mail: xingshanghua@126.com

The ORCID identification number(s) for the author(s) of this article can be found under https://doi.org/10.1002/adfm.202503013

DOI: 10.1002/adfm.202503013

A. Mohabbat, I. Boldog, T. Heinen, C. Janiak
Institut für Anorganische Chemie und Strukturchemie
Heinrich-Heine-Universität Düsseldorf
40225 Düsseldorf, Germany
E-mail: janiak@hhu.de

J. Möllmer, M. Lange
Institut für Nichtklassische Chemie e.V.
Permoserstraße 15, 04318 Leipzig, Germany

Y. Haiduk, V. Pankov
Belarusian State University
Leningradskaya str.14, Minsk 220050, Belarus

O. Weingart
Institut für Theoretische Chemie und Computerchemie
Heinrich-Heine-Universität Düsseldorf
40225 Düsseldorf, Germany

corrosive nature of the adsorbate,[9–13] exacerbated by the need for maximally complete separation of SO_2 at low concentrations (< 500 ppm), particularly in the presence of CO_2, the dominant adsorptive-competitor in flue gases.[14–17]

Rational design approaches toward the synthesis of stable MOFs for selective SO_2 adsorption presents an interesting challenge. Typically, the use of open metal sites or highly polar groups, decorating the pore surface, have been employed to improve SO_2 affinity.[1,18] However, even the pore-size tuning itself, aiming at an approximate optimum at 4–8 Å (i.e., a size range, which only slightly exceeds the 4.1 Å kinetic diameter of the SO_2 molecule) could radically improve the physisorption of SO_2, as demonstrated by us recently.[19] The reliance on pore-size optimization improves the opportunities to target maximally stable MOFs without chemical moieties that compromise the stability of the framework.

So far, most of the MOF research toward SO_2 has nearly solely focused on capture/separation as a goal. Particularly, fluorinated MOFs, KAUST-7 ($[Ni(NbOF_5)(pyrazine)_2]\cdot 2H_2O$) and KAUST-8 ($[Ni(AlF_5(OH_2))(pyrazine)_2]\cdot 2H_2O$) revealed the selective capture of SO_2 and were able to detect SO_2 at low concentration of 25–500 ppm.[17] The possibility to use a MOF as a sensor for SO_2 detection is a yet to-be-developed related research target.[20] The key property of a potential SO_2 sensor is high and selective SO_2 adsorption at low partial pressures (0.001–0.05 bars; typical concentrations of concern start at ppm concentration levels); as for a sensor, the total SO_2 uptake becomes irrelevant. The electronic state of MOF materials can be influenced by SO_2 adsorption through the intermolecular interactions, which changes the electrical resistivity thereby allowing signal detection. In general, MOFs are poor electric conductors and rarely form a continuous conducting circuit, since conjugated π-bonded arene fragments, are interrupted by σ bonding, which generally does not support electron mobility.[21] However, a MOF potentially could be a good resistive sensor: the adsorbed SO_2 molecules might change slightly the electronic state of the framework, which could translate into a significant change for a weakly conductive MOF.

Herein, we synthesized a series of stable MOFs with varying pore sizes aiming for the optimization of SO_2 separation from N_2/CO_2. The "pillared" DMOFs,[22] $[Ni_2L_2(DABCO)]$, where L = 1,4-benzenedicarboxylate (BDC), 1,4-naphthalenedicarboxylate (NDC), 2,6-naphthalenedicarboxylate, 9,10-anthracendicarboxylate (ADC), and 1,4-diazabicyclo[2,2,2]octane (DABCO) were deemed an excellent series for optimization of SO_2 adsorption through vdW interactions (**Figure 1**). The tuning offers pore diameters in the range of 4–9 Å and pore environments with large areas belonging to aromatic moieties, beneficial either for improved physisorption energetics, as well as chemiresistive sensing via interactions with SO_2 and hydrolytic stability due to their hydrophobicity. To the best of our knowledge, this is the first work of fine-tuning a MOF's micropore geometry to improve SO_2 trace adsorption and SO_2/CO_2 selectivity.

2. Results and Discussion

In DMOF structures, the $\{Ni_2\}$ paddle wheel units are connected by dicarboxylic linkers (L) to yield 2D square grids $\{Ni_2(L)_2\}$, which are further pillared by DABCO linkers resulting in 3D

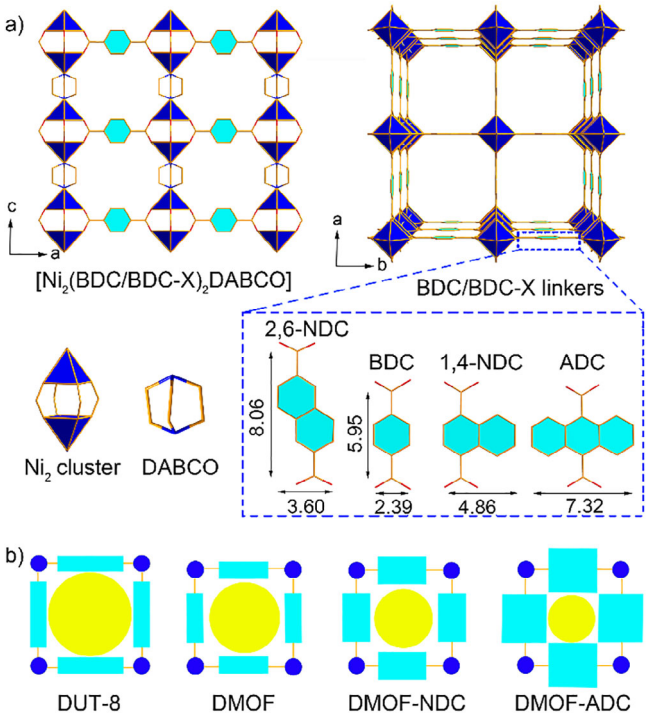

Figure 1. a) Top row: views on the porous DMOF-type structures along the *a*/*b*-axis (left) and along the c-axis (right). Bottom row: The $\{Ni_2\}$ cluster, and the ligands constituting the DMOF-type MOFs in this work. Hydrogen atoms are omitted for clarity. b) Schematic representation of the gradually shrinking pore apertures resulting from the use of linkers of increasing bulkiness.

frameworks. The pore size within this family of materials can be systematically tuned by changing the size (length and width) of the dicarboxylate linkers. In the progenitor of the DMOF series, the $[Ni_2(BDC)_2(DABCO)]$, wide 7.5 × 7.5 Å^2 square channels run along the *c*-axis, while narrower 5.0 × 3.5 Å^2 channels, running along the *a*- and *b*-axis, connect the former to a 3D pore system (Figure 1a). By using the bulkier 1,4-NDC and ADC linkers instead of BDC, the pore size in the resulting structures of DMOF-NDC and DMOF-ADC narrows down (Figure 1b) to ultra-microporous in DMOF-ADC (4.4 × 4.4 Å^2), according to the structural data (Figure S1, Supporting Information). Alternatively, when the longer 2,6-NDC linker was used in DUT-8, the pore size increased to 9 × 9 Å^2. The decrease of pore sizes was experimentally demonstrated by Ar sorption experiments (87 K), with primary micropore sizes in the quenched solid density functional theory (QSDFT-)based distribution from 9.2 Å for DUT-8 to ≈5.4 Å for DMOF-ADC (**Figure 2**). For the structure of DMOF-NDC and DMOF-ADC, the carboxy groups are out of the plane of naphthalene/anthracene rings due to the steric effect of linker bulkiness (Figure S1, Supporting Information). Thereby, the pore aperture size of DMOF-NDC is highly affected by the tilting direction of the naphthalene plane and varies between ≈6.0 × 6.0 Å^2 and ≈4.4 × 4.4 Å^2 (Figure S1, Supporting Information).

The powder X-ray diffractograms (PXRD) of DUT-8, DMOF, DMOF-NDC, and DMOF-ADC match with their respective simulated PXRD patterns (Figure S2, Supporting Information) from X-ray crystal structures. The expected 2:1 molar ratio of L to

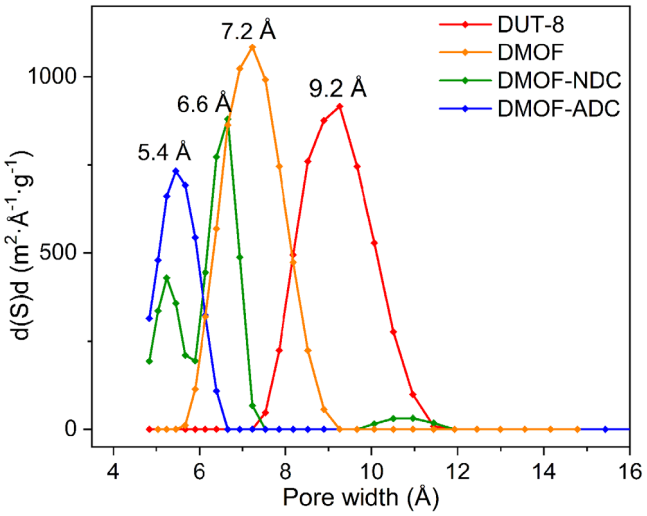

Figure 2. Pore size distribution of DUT-8, DMOF, DMOF-NDC, and DMOF-ADC determined from Ar sorption at 87 K. The pore size distribution was calculated using a QSDFT model (Ar adsorption data at 87 K, carbon QSDFT, slit pore, QSDFT equilibrium model).

DABCO linker based on the formula of $[Ni_2(L)_2DABCO]$ was confirmed by ^1H·NMR spectra of the digested samples (Figures S5–S8, Supporting Information), being consistent with the results of the elemental analysis (Section S2, Supporting Information). All materials were stable up to 300 °C from the thermogravimetric analysis (TGA, Figure S4, Supporting Information). The porosities of the DMOF materials were investigated by N_2 and Ar sorption isotherms at 77 and 87 K (Figure S10, Supporting Information). The Brunauer–Emmett–Teller (BET) surface area and pore volume were found to decrease in the order of DUT-8 > DMOF > DMOF-NDC > DMOF-ADC, according to the shortening of the ligand and the increase of its bulkiness (**Table 1**). The calculated pore size distribution (based on Ar adsorption at 87 K), DUT-8, DMOF, DMOF-NDC, and DMOF-ADC exhibited pore widths ≈9.2, 7.2, 6.6/5.2, and 5.4 Å, respectively (Figure 2), in good agreement with the results from the structure analysis (Figure S1, Supporting Information). DMOF-NDC showed two micropore widths ≈6.6 and 5.2 Å, as a result of the tilted disposition of the naphthalene rings.

The SO_2 adsorption isotherms of DUT-8, DMOF, DMOF-NDC, and DMOF-ADC were explored at 293 K. At 0.97 bar, the SO_2 adsorption capacities of DUT-8, DMOF, DMOF-NDC, and DMOF-ADC were 13.99, 13.09, 10.09, and 6.51 mmol g^{-1}, respectively, showing an expected linear correlation with the BET surface area and total pore volume (Figures S10 and S11, Supporting Information). However, the SO_2 uptake at low-pressure is nearly independent of surface area and pore volume. As shown in **Figure 3**, at a low-pressure of ≈0.01 bar, DMOF-ADC and DMOF-NDC with narrow pores show significantly higher SO_2 uptakes than DMOF and DUT-8 with wide pores (1.90 mmol g^{-1} for DMOF-ADC and 1.39 mmol g^{-1} for DMOF-NDC vs 0.26 mmol g^{-1} for DMOF and 0.27 mmol g^{-1} for DUT-8). Notably, the SO_2 uptake for DMOF-ADC at 293 K and 0.01 bar surpass the uptake in some well-known MOFs with open metal sites or polar functional groups, such as Zr-Fum (1.3 mmol g^{-1}),[19] NH_2-MIL-101-Al (1.5 mmol g^{-1}),[19] MIL-53-Al (0.4 mmol g^{-1}),[19] MOF-177 (0.3 mmol g^{-1}),[15] and SIFSIX-3-Zn (1.68 mmol g^{-1}).[14] As the pressure increased to ≈0.05 bar, the SO_2 uptakes of DMOF-ADC (3.36 mmol g^{-1}) and DMOF-NDC (3.87 mmol g^{-1}) were still higher than those of DMOF (1.32 mmol g^{-1}) and DUT-8 (0.95 mmol g^{-1}). The obvious enhancement of the low-pressure SO_2 uptake from DUT-8 and DMOF to DMOF-NDC and DMOF-ADC can be attributed to the narrowing of the pores, which facilitate the multi-site interaction between SO_2 and the inner pore surface. This interaction is further reflected by the isosteric enthalpy of SO_2 adsorption ($-\Delta H_{ads}$) from virial analysis (Figures S16–S19, Supporting Information).[27] The $-\Delta H_{ads}$ values near zero coverage ($-\Delta H_{ads}{}^0$) in DUT-8, DMOF, DMOF-NDC, and DMOF-ADC were 21, 33, 39, and 54 kJ mol^{-1}, respectively (Figure S24, Supporting Information). In addition, when the SO_2 uptakes

Table 1. Specific surface area, pore volume, and SO_2 uptake of DMOF derivatives.

Material	BET-surface area [a] (N_2/Ar) [m^2 g^{-1}]	Total pore volume [b] (N_2/Ar) [cm^3 g^{-1}]	Pore width[c] [Å]	SO_2-uptake at the given pressure (in bar) at 293 K [mmol g^{-1}] (g g^{-1}) [e]			
				0.01	0.05	0.1	0.97
DUT-8	2184/2274	0.99/0.91	9.2	0.27	0.95	2.25	13.99 (0.89)
DMOF	1957/1944	0.76/0.70	7.2	0.26	1.32	7.21	13.09 (0.84)
DMOF-NDC	1139/970	0.44/0.36	6.6, 5.2	1.39	3.87	5.29	10.09 (0.65)
DMOF-ADC	799/781	0.31/0.32	5.4	1.90	3.36	4.44	6.51 (0.42)
DUT-8 Lit.[23]	2440/–	1.12/–	–	–	–	–	–
DMOF Lit.[24]	2050/–	0.80/–	7.5, 5.3 × 6.9[22], [d]	–	–	–	≈9.97 [e]
(Zn)DMOF-NDC Lit.[25]	1414/–	0.51/–	–	–	–	–	≈5.0 [e]
(Zn)DMOF-ADC Lit.[26]	728/–	0.29/–	–	–	–	–	≈7.0 [e]

[a] Obtained from five adsorption points in the pressure range $0.001 < P\,P_0^{-1} < 0.05$; [b] Derived at $P\,P_0^{-1} = 0.9$; [c] Pore widths from pore size distribution are measured by Ar sorption at 87 K; [d] From X-ray structure; [e] Uptake in $g\,g^{-1} = 0.064\ g\ mmol^{-1} \times$ uptake in mmol g^{-1}; [f] SO_2 uptake at ≈1 bar was roughly estimated from the SO_2 adsorption isotherm at 298 K from reference.

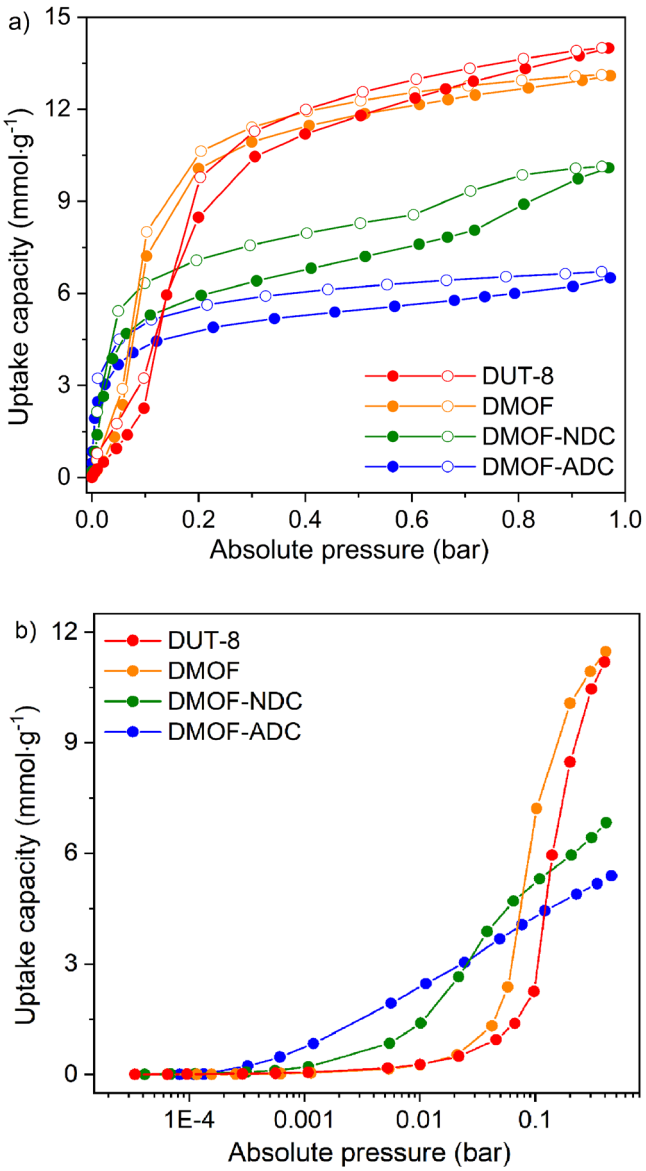

Figure 3. a) SO_2 sorption isotherms of DUT-8, DMOF, DMOF-NDC and DMOF-ADC at 293 K between 0 and 0.97 bar; b) The enlarged SO_2 adsorption at low-pressure of 0–0.4 bar for better visibility of the onset of the steep uptake. Filled and open symbols indicate the adsorption and desorption isotherms, respectively.

at low-pressure of 0.01 and 0.1 bar were normalized by the BET surface area, the resulting surface-specific SO_2 uptake against the pore width shows an obvious maximum for DMOF-ADC and DMOF-NDC in **Figure** 4. As the pore width reaches an optimal value with ≈4.4 Å, which approaches the kinetic diameter of SO_2 (4.1 Å), DMOF-ADC shows the best performance at 0.01 bar. Interestingly, DMOF-NDC is very close in the low-pressure uptake and in the surface-specific uptake at 0.1 bar to DMOF-ADC as parts of its pores are similarly narrow as in DMOF-ADC because of the tilting (see above, Figure 2; Figure S1, Supporting Information).

Previous work by Eddaoudi et al. found a preferred H_2S adsorption on rare earth-based MOFs with the NDC linker compared to isostructural MOFs with fumarate and 2-fluoro-4-(1H-tetrazol-5-yl) benzoate linkers. This preferred adsorption was attributed to the narrower pore system formed with the NDC linker and hence, the stronger framework-H_2S interactions.[28]

Based on the specific SO_2 uptake at 0.97 bar and 293 K (in g g^{-1}) and (its division by) the specific total pore volumes of the DMOFs from N_2 sorption (Table 1), SO_2 packing densities (in g cm^{-3}) of 0.9 in DUT-8, 1.1 in DMOF, 1.48 in DMOF-NDC, and 1.35 in DMOF-ADC are calculated, which show the efficient SO_2 packing in DMOF-NDC and -ADC comparable with the packing densities of liquid SO_2 of 1.46 g cm^{-3} at 263 K and 1 bar[29] and gaseous SO_2 of 2.619 g dm^{-3} at 293 K and 1 bar.[29]

DFT-D (dispersion-corrected DFT) calculations were performed to probe the effect of pore dimension on the interaction of SO_2 with the inner surface of the DMOFs. Two DFT system models on DUT-8, DMOF, DMOF-NDC, and DMOF-ADC were isolated from their respective X-ray crystal structure (Section S7 and Figure S40, Supporting Information), which resemble the different local pore surface environment (along *a*/*b*-axis and *c*-axis). For DMOF-ADC and DMOF-NDC, the available data from the known isostructural Zn analogs were used. The trapped SO_2 molecule was primarily bound through arene-$\pi^{(\delta-)}$...$^{(\delta+)}$S and (C)H$^{(\delta+)}$...$^{(\delta-)}$O(S) interactions with the aromatic and DABCO linkers (**Figure** 5; Figure S42, Supporting Information). The arene-$\pi^{(\delta-)}$...$^{(\delta+)}$S distances of DMOF-NDC and DMOF-ADC are 3.67 and 3.61 Å, respectively. These distance values are much shorter than the sum of the CAr and S atom's vdW radii (3.91 Å). The SO_2 adsorption seems weaker in wider-pore materials of DMOF and DUT-8, implied by the longer arene-$\pi^{(\delta-)}$...$^{(\delta+)}$S distances of 4.01 and 4.13 Å, respectively, compared to DMOF-ADC and DMOF-NDC (Figure 5). The reduced strength of arene-$\pi^{(\delta-)}$...$^{(\delta+)}$S interactions in DMOF and DUT-8 was further corroborated by the determined SO_2 binding energies (Table S3, Supporting Information). The SO_2 binding energies in DMOF-ADC

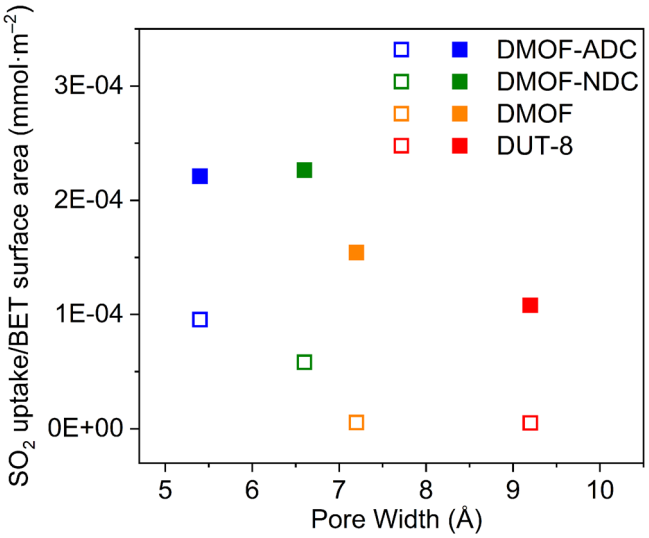

Figure 4. Surface-specific SO_2 uptake at 0.01 bar (open symbols) and 0.1 bar (closed symbols) (293 K), which is the uptake at this pressure divided by the BET-surface area versus the pore limiting diameter (PLD).

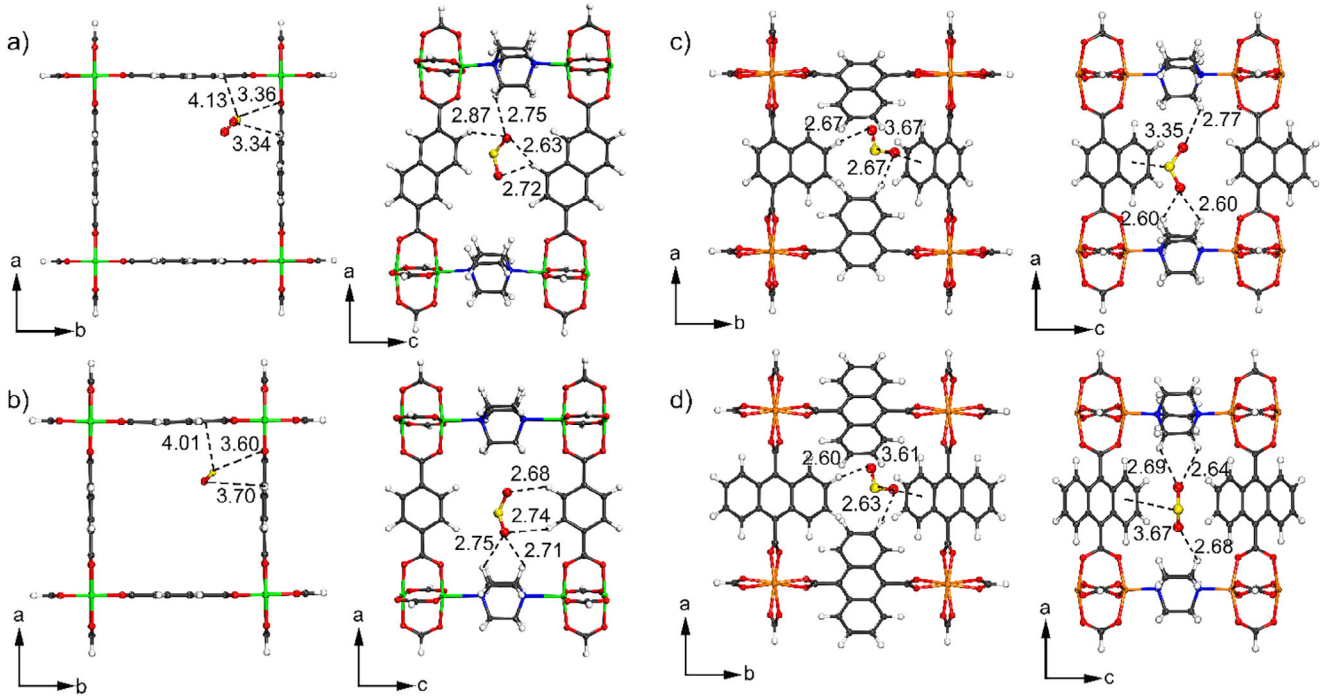

Figure 5. a–d) DFT-D calculated SO_2 binding sites for the optimized DMOF-ADC (a), DMOF-NDC (b), DMOF (c), and DUT-8 (d). The left and right images are the views of the structure along the *c*-axis, and along the *a*- or *b*-axis, respectively (cf. Figure 1). For DMOF-ADC and DMOF-NDC, the structure models from the known isostructural Zn analogs were used for DFT optimization as there is no reported crystal structure for Ni-based DMOF-ADC and DMOF-NDC. The distances are given in Å. The calculation details are provided in Section S7 (Supporting Information). Color code: S, yellow; O, red; N, blue; Ni, green; Zn, orange; C, gray; H, light gray.

and DMOF-NDC were obviously higher than those in DMOF and DUT-8, in line with the experimental $-\Delta H_{ads}$ results for SO_2.

It should be noted that the pores of DMOF-ADC could accommodate at least six SO_2 molecules, which was demonstrated by periodic DFT-D calculations (**Figure 6**). All SO_2 molecules are mainly located in close proximity between the ADC linkers and held by multi-site MOF-SO_2 interactions, while simultaneously interacting with other SO_2 molecules by $SO_2{}^{(\delta-)}\cdots{}^{(\delta+)}SO_2$ dipole-dipole interactions. The intermolecular distances in adsorbed SO_2 molecules are in the range of 2.8–3.6 Å (Figure 6), which are shorter than the sum of the vdW radii of S and O atoms (3.67 Å). These short distances indicate the efficient dense SO_2 packing within the narrow pores of DMOF-ADC. In addition, the binding energies are increasing with the SO_2 loading. The binding energies in DMOF-ADC with two, four, and six SO_2 molecules are determined to be 46, 49, and 53 kJ mol^{-1}, respectively.

To shed light on the location of SO_2 within the pores of DMOF-ADC, powder XRD studies of SO_2-loaded DMOF-ADC were performed (details in Section S9 and Figures S44–S48, Supporting Information). The cell volume of the framework upon SO_2 adsorption remains the same with less than 0.1% volume change (Table S4, Supporting Information), reflecting the rigidity of the framework. However, the anthracene moiety of the ADC ligand demonstrates a significant rotation out of the planes of the carboxylate moieties upon SO_2 adsorption (≈48° vs 75° for DMOF-ADC versus DMOF-ADC-SO_2, Figure S45, Supporting Information). Notably, the majority of SO_2 molecules are pointed to the anthracene group of the ADC ligand with multiple O-π interactions (Figure S48, Supporting Information), as the SO_2 loading is maximized at 100 K, the $S^{(\delta+)}\cdots{}^{(\delta-)}O$ contacts between the SO_2 molecules seem to be of high significance. We trace the difference in the dominant intermolecular interactions compared to the calculations and the generally expected situation for low loading of SO_2 to this factor. In any case, the positions of the guest molecules are determined with low precision due to the high refined thermal displacement factors; hence, the result should be viewed rather as a distribution statistic, with some interesting secondary observations given in the SI.

We further investigated the vibrational modes of SO_2 loaded DMOF-ADC upon the exposure to air atmosphere (during 1–10 min). Two new bands at 1143 and 1340 cm^{-1}, associated with vibrational stretching of the adsorbed SO_2 molecules, appeared, which were not observed in the pristine DMOF-ADC (Figure S43, Supporting Information). These bands gradually disappeared upon air exposure over 10 min.

Considering CO_2 as the main competing gas during the desulfurization process, the CO_2 adsorption isotherms on DMOFs materials were also collected at 293 K (Figures S12–S15, Supporting Information). The narrowing pore structure also contributes to an enhanced low-pressure CO_2 adsorption from DUT-8 to DMOF-ADC (Table S1, Supporting Information). However, the increase of low-pressure SO_2 uptake is much higher than that of CO_2, especially in DMOF-NDC and DMOF-ADC. For example, at ≈0.01 bar, which is a model pressure for investigating trace SO_2 capture from a SO_2/CO_2 mixture (1/99, v/v), the SO_2 and CO_2 uptakes by DUT-8, DMOF, DMOF-NDC, and DMOF-ADC are 0.27 and 0.019 mmol g^{-1}, 0.26 and 0.018 mmol g^{-1}, 1.39 and 0.045 mmol g^{-1}, and 1.90 and 0.061 mmol g^{-1}, respectively.

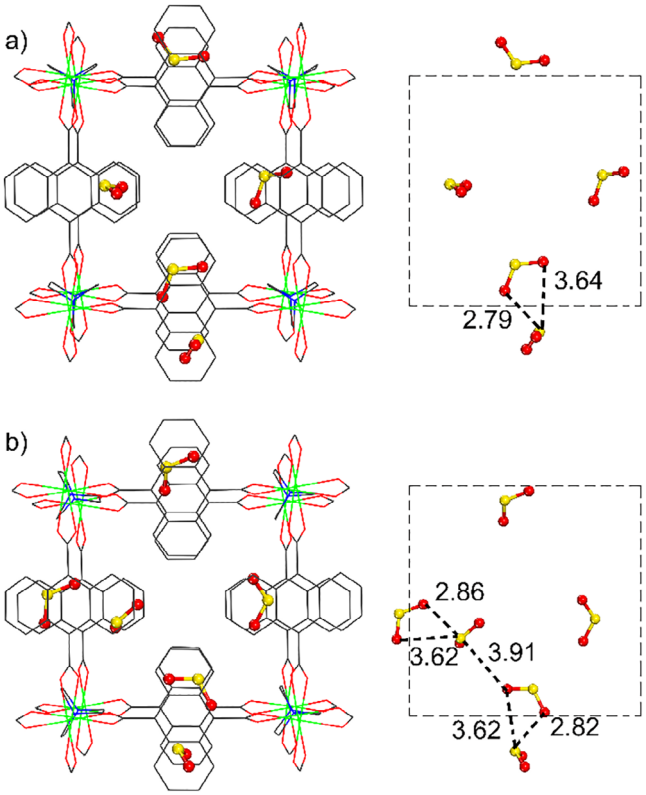

Figure 6. Periodic DFT-D calculated structures of DMOF-ADC (Ni) with five (Figure 6a) and six (Figure 6b) molecules of SO_2. Hydrogen atoms on framework images are omitted for clarity. The distances are given in Å.

This was attributed to the difference in polarizabilities (47.7×10^{-25} cm^3 vs 29.1×10^{-25} cm^3) and dipole moments (1.62 D vs 0 D) between SO_2 and CO_2. The higher affinity of the DMOFs for SO_2 over CO_2 was further reflected by the higher $-\Delta H_{ads}$ values (Figure S25, Supporting Information) and by the higher SO_2 binding energies (Figure S35 and Table S3, Supporting Information). Additionally, the CH_4 and N_2 uptake at low-pressures (0.01 and 0.1 bar) and at 0.97 bar are far below those for SO_2 (Table S1, Supporting Information).

Dynamic transient breakthrough experiments were further carried out to evaluate the actual separation performance of $N_2/CO_2/SO_2$ mixtures (84:15:1 v/v/v) containing 10 000 ppm SO_2 at 293 K and 1 bar (experimental details given in Section S6, Supporting Information). From breakthrough curves (**Figure 7**), CO_2 and N_2 were eluted through the fixed-bed immediately, but SO_2 could be retained for ≈87 and ≈57 min g^{-1} in DMOF-ADC and DMOF-NDC samples, respectively. The separation performance of DMOF-ADC was better than DMOF-NDC, in line with the results from adsorption isotherms and ideal adsorbed solution theory (IAST) calculations (Section S4.2 and Table S2, Supporting Information). As expected, the dynamic SO_2 loadings of DMOF-ADC and DMOF-NDC in the breakthrough experiment (293 K, 1% SO_2) were similar to their static SO_2 capacities (2.00 vs 1.90 mmol g^{-1} for DMOF-ADC, 1.16 vs 1.39 mmol g^{-1} for DMOF-NDC) in single-component gas isotherms at 293 K and 0.01 bar, even in the presence of competing molecules of CO_2. Then, multiple-breakthrough cycling tests were performed to evaluate the recyclability of the $SO_2/CO_2/N_2$ separation. The separation performance of DMOF-ADC and DMOF-NDC could be recycled at least over four continuous runs with nearly unchanged SO_2 retention times (Figures S38 and S39, Supporting Information).

DMOF-NDC and -ADC also exhibits CO_2/N_2 selectivity as seen from the higher CO_2 uptake over N_2 (Table S1, Supporting Information) and from the breakthrough experiments for the separation of the $N_2/CO_2/SO_2$ mixture (84:15:1 v/v/v), where an immediate composition of 100% N_2 was found in the outlet, while CO_2 was eluted with retention times of ≈15 min g^{-1}.

The majority of anthropogenic SO_2 emission emerges from combustion of coal and heavy oil or is caused by industrial processes. The SO_2 content in flue gases is relatively low (the typical

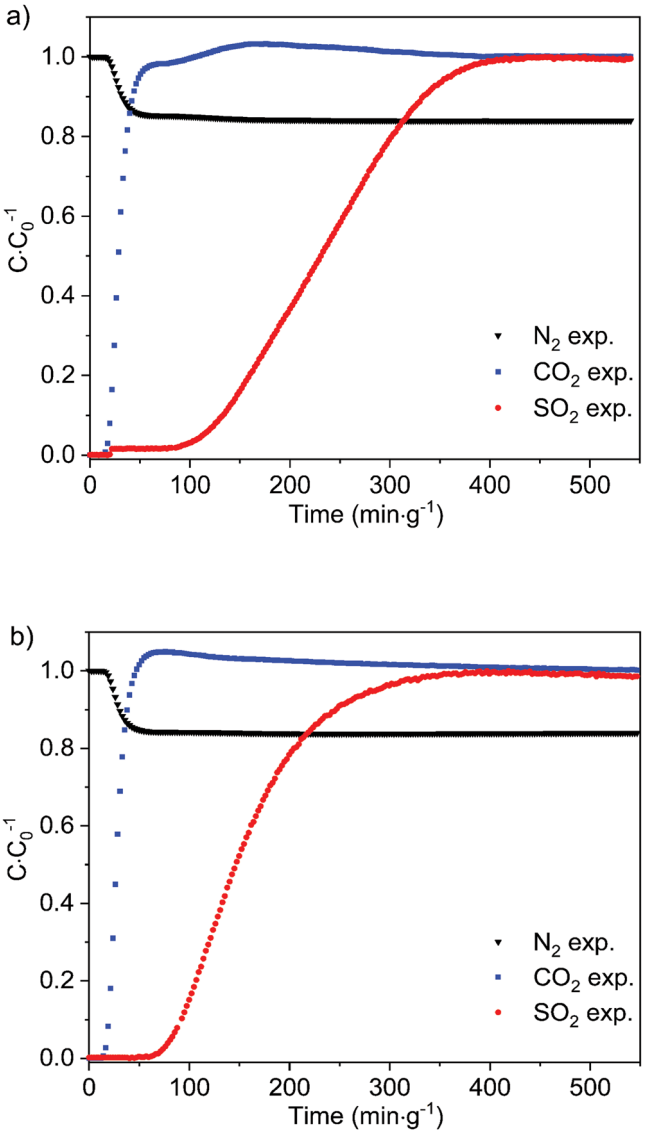

Figure 7. a,b) Experimental breakthrough curves of DMOF-ADC (a) and DMOF-NDC (b) for the separation of $N_2/CO_2/SO_2$ mixtures (84:15:1 v/v/v) at 293 K and 1 bar.

composition of flue gas: N_2 = 70–75%; CO_2 = 10–15%; SO_2 = 500–3000 ppm), and large parts of it (85–95%) can be scrubbed with classic flue gas desulfurization, using limestone as an absorbent. The desulfurization of flue gas is a step before a potential future CO_2 scrubbing process in test plants. Residual SO_2 in post-combustion flue gas can react with organic amines in the CO_2 scrubbing process, causing permanent loss of amine activity and decreasing the efficiency of this process. Considering the acidic nature of both SO_2 and CO_2 molecules and the much lower SO_2 concentration in flue gas than CO_2, it is of significance to effectively remove trace SO_2 from CO_2 with a SO_2/CO_2 selectivity much larger than 1. Also, for SO_2 adsorption from other processes such as H_2SO_4 production, the fraction of SO_2 (≈500 ppm) in air is close to that of CO_2 (≈400 ppm). Again, the selectivity of SO_2/CO_2 must be larger than 1 to ensure successful SO_2 adsorption.

The stability of DMOF materials under dry SO_2 (static adsorption measurement, ≈6 h) and humid SO_2 exposure treatments (35 ppm SO_2 content in the air atmosphere with 75% relative humidity, RH, for 6 h) were tested. The integrity of crystallinity and porosity after stability tests was evaluated by PXRD and porosity measurement by N_2 sorption at 77 K. The nearly unchanged PXRD patterns for all DMOFs materials before and after dry SO_2 exposure indicate the retained crystallinity without phase transformation and degradation (Section S5 and Figures S27 and S28, Supporting Information). But after humid SO_2 exposure, only DMOF-ADC remained crystalline (and in part DMOF). Furthermore, only DMOF-ADC showed an unchanged BET surface area after dry and humid SO_2 exposure (Figures S29–S32, Supporting Information). The surface area of DMOF-NDC was retained under dry SO_2 exposure, but degraded under humid SO_2 exposure (Figure S31, Supporting Information). For DMOF and DUT-8, a significant decrease in surface area was already observed after dry SO_2 treatment (Figures S29 and S30, Supporting Information). The regeneration ability of DMOF-ADC was further evaluated by recycling dry and humid SO_2. Remarkably, the SO_2 uptake capacity of regenerated DMOF-ADC can almost be retained for at least five runs of SO_2 adsorption (Figure S33, Supporting Information). The crystallinity of DMOF-ADC after the 5th dry and humid SO_2 sorption cycle remained unchanged, albeit with a slightly reduced BET surface area (Figures S34–S37, Supporting Information).

Only a few electrochemical MOF sensors and other semiconductor-based materials have been reported for SO_2 detection.[30–32] The MOF [Ni_2(DOBPDC)] (DOBPDC = 4,4-dioxidobiphenyl- 3,3-dicarboxylate) exhibits a broad emission band at 450 nm (350 nm irradiation) and when exposed to SO_2, the emission peak shifts to 405 nm with a 61% increase in emission intensity even at a low SO_2 pressure of 0.1 bar.[32] The above noted isostructural fluorinated MOFs KAUST-7 ([$Ni(NbOF_5)(pyrazine)_2$]·$2H_2O$) and KAUST-8 ([$Ni(AlF_5(OH_2))(pyrazine)_2$]·$2H_2O$) were employed for SO_2 sensing as coatings on a quartz-crystal microbalance, QCM (in a SO_2/N_2 mixture).[17] Based on the change in frequency of the QCM resonator, SO_2 was successfully detected at concentrations between 25 and 500 ppm. Under 60% relative humidity in synthetic air, the KAUST-7 sensor was not significantly affected, however, for KAUST-8 a much lower sensitivity to SO_2 was observed. The stability and reproducibility of the system was

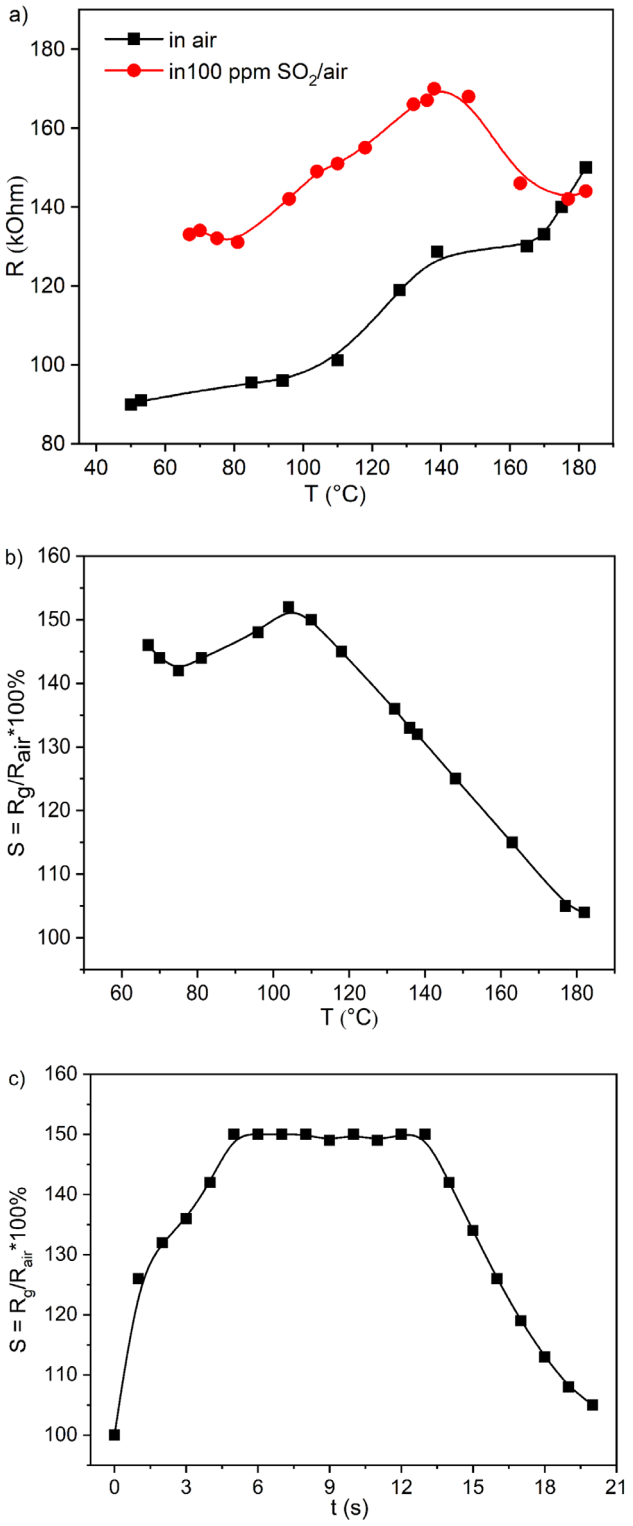

Figure 8. The sensitivity of a sensor prototype in the form of a DMOF-ADC tablet (pellet) pressed from powder (see Section S10, Supporting Information for details) toward an SO_2-air mixture containing 100 ppm SO_2. a) The absolute value of tablet resistance in a gas-air mixture and in air; b) sensory response $S = R_g/R_{air} \times 100\%$ (the g subscript corresponds to the SO_2/air mixture); c) dependence of the sensory response on the time of exposure to the gas-air mixture at 80 °C.

shown for up to 12 days when exposed to up to 157 ppm of dry SO_2.[17]

A composite of the MOF nickel benzene-tricarboxylate (Ni_3BTC_2) and OH-functionalized single-walled carbon nanotubes (OH-SWNTs) was investigated in a chemically sensitive field-effect transistor (ChemFET) with a response time of 11 s at 15 ppm SO_2,[33] a resistance change with a response time of 10 s and recovery time of 30 s at 1 ppm SO_2.[34] Further, UiO-66-NH_2 was incorporated in a capacitive sensor in a nanofiber membrane, using polyvinylidene fluoride (PVDF) and carbon nanotubes (CNT) for real-time monitoring of SO_2 with response times of 435 and 185 s at 150 and 1 ppm SO_2, respectively.[35] UiO-66-NH_2 was also embedded into electrospun polyacrylonitrile (PAN) nanofibers, equipped with CNT electrodes to measure concentrations of down to 1 ppm of SO_2 with a response time of 255 s.[36] When UiO-66-NH_2 was loaded with PAN via an in-situ growth mechanism and modified with 2,3,4-trihydroxy benzaldehyde (THBA), the resultant UiO-66-THBA/PAN-based capacitive gas sensor reached a detection limit of 0.1 ppm.[37] For the MOF MFM-300(In)-coated interdigitated electrodes (IDEs) the measured capacitance changes were in the SO_2 concentration range between 75 and 1000 ppb with the detection limit as low as 5 ppb.[38]

The UiO-66 derivatives UiO-66-NH_2 and UiO-66-OH were tested as chemoresistive sensors for SO_2, NO_2, and CO_2 in a mixture with N_2 or Ar (for CO_2).[39] Parent UiO-66 does not exhibit a change in resistance after exposure to any of the acidic gases listed above. However, UiO-66-NH_2 responded with a 22 ± 3% resistance change for 10 ppm SO_2, with a 1 ppm limit of detection (response of 3.2 ± 0.2%). This SO_2 performance was much higher than for 10 pm NO_2 with 7.6 ± 0.4% and much higher than for CO_2 with 11 ± 2%, albeit at 5000 ppm, and was attributed to the formation of a charge-transfer complex of SO_2 with the amine groups in the BDC-NH_2 linker.[39] The commercial Dräger Pac 6000 SO_2-detector can detect SO_2 within the range of 0–100 ppm and the operating temperature range is −30–50 °C.[40]

According to the adsorption studies and SO_2 exposure experiments discussed above, the DMOF-ADC has superior selective SO_2 adsorption performance and, at the same time, remains stable under dry and humid SO_2 conditions. Thus, the SO_2 sensing capabilities in air was explored using a DMOF-ADC sample. The experimentally observed increase in the resistance of the MOF-ADC sample in the 60–150 °C temperature range indicates that the dispersion interaction between SO_2 and fragments of the linker chain, which is responsible for changing the dielectric characteristics of the medium, leads to a decrease in the electron mobility. The intermolecular interaction between SO_2 molecules and CH groups of the arene ring/arene-π, as noted earlier, can noticeably change the electrical resistance of the MOF. It is assumed that when the pores are empty, the conductivity could evidently be described via electrons "hopping" from one metal atom via the aryl core of the ligand, representing a conjugated π-system, to another metal atom (Figure S51, Supporting Information). Thereby the conductivity of the ligand is viewed as the limiting stage in the electron conductivity via hopping and the presence of SO_2 in the pores significantly affects the overall conductivity.

At temperatures above 150 °C, the effect of SO_2 adsorption on the mobility of charge carriers decreased, and after 180 °C, the opposite effect is, seemingly, observed (**Figure** 8a). The largest difference between the resistance of the sample in a 100 ppm SO_2/air medium and neat air was 152% at a temperature of 104 °C (Figure 8b). In comparison, the response speed of the sensor element at 100 °C (time to reach the maximum signal) was 4–5 s, and the recovery time was 4–7 s (Figure 8c). The reversibility of the electrical resistance of the MOF-ADC sample with respect to 100 ppm SO_2/air medium was also established. The observations demonstrate the prospects of building a resistive SO_2 sensor based on the DMOF-ADC material.

3. Conclusion

A strategy for optimizing the pore environment of MOFs to achieve an enhanced SO_2 separation and SO_2 chemiresistive sensing performance was successfully demonstrated. The hydrophobicity, and hence the resistance to the corrosion by wet SO_2, was ensured by expansion of the BDC ligand with conjugated benzene rings. The optimal match of the MOF's pore channel with the 4–5 Å kinetic diameter of SO_2 was achieved in DMOF-ADC, providing a highly stable SO_2 separation performance with a cycling breakthrough SO_2 capacity of ≈2.0 mmol g^{-1} for 1% SO_2 in an N_2/CO_2 (84/15 v/v) mixture. The DFT calculations reveal that the optimal pore size of DMOF-ADC by linker rotation enables multiple cooperative SO_2 interactions with the framework in close proximity, which is the basis for a high SO_2 affinity and efficient capture. Furthermore, DMOF-ADC gave a good chemiresistive sensing for SO_2 at 100 ppm. This work demonstrates an application of general strategy toward the optimization of pore environments for designing porous materials regarding task-specific applications by fine-tuning the pore sizes to optimal match with the kinetic diameter of the gas molecule of interest (the generally high stability of the chosen MOF platform featuring ligands with large aromatic cores are the particular features, which made the realization of the general strategy particularly successful in the case of the highly corrosive SO_2 gas).

Supporting Information

Supporting Information is available from the Wiley Online Library or from the author.

Acknowledgements

The authors gratefully acknowledge the support from National Natural Science Foundation of China (No. 32302234) and Liaoning Province Natural Science Foundation Joint Fund Plan (No. 2024-MSLH-022). The research was funded by the Deutsche Forschungsgemeinschaft (DFG) within the Priority Program SPP 1928/2 COORNETs (grant Ja466/43-1) and in part through the Deutscher Akademischer Austauschdienst (project 57724286, "Metal–organic frameworks for volatile organic compound sensing").

Open access funding enabled and organized by Projekt DEAL.

Conflict of Interest

The authors declare no conflict of interest.

Data Availability Statement

The data that support the findings of this study are available in the supplementary material of this article.

Keywords

adsorption, metal–organic frameworks, pore environment tuning, sensing, SO_2 separation

Received: February 1, 2025
Revised: March 3, 2025
Published online:

[1] T. Islamoglu, Z. Chen, M. C. Wasson, C. T. Buru, K. O. Kirlikovali, U. Afrin, M. R. Mian, O. K. Farha, *Chem. Rev.* **2020**, *120*, 8130.
[2] N. S. Bobbitt, M. L. Mendonca, A. J. Howarth, T. Islamoglu, J. T. Hupp, O. K. Farha, R. Q. Snurr, *Chem. Soc. Rev.* **2017**, *46*, 3357.
[3] X. Han, S. Yang, M. Schröder, *Nat. Rev. Chem.* **2019**, *3*, 108.
[4] E. Martinez-Ahumada, M. L. Diaz-Ramirez, M. J. Velasquez-Hernandez, V. Jancik, I. A. Ibarra, *Chem. Sci.* **2021**, *12*, 6772.
[5] H. Yuan, N. Li, W. Fan, H. Cai, D. Zhao, *Adv. Sci.* **2022**, *9*, 2104374.
[6] J. Wang, Y. Zhang, Y. Su, X. Liu, P. Zhang, R. B. Lin, S. Chen, Q. Deng, Z. Zeng, S. Deng, B. Chen, *Nat. Commun.* **2022**, *13*, 200.
[7] J. Zhou, T. Ke, F. Steinke, N. Stock, Z. Zhang, Z. Bao, X. He, Q. Ren, Q. Yang, *J. Am. Chem. Soc.* **2022**, *144*, 14322.
[8] K. Shao, H. M. Wen, C. C. Liang, X. Xiao, X. W. Gu, B. Chen, G. Qian, B. Li, *Angew. Chem. Int. Ed. Engl.* **2022**, *61*, 202211523.
[9] J. Li, G. L. Smith, Y. Chen, Y. Ma, M. Kippax-Jones, M. Fan, W. Lu, M. D. Frogley, G. Cinque, S. J. Day, S. P. Thompson, Y. Cheng, L. L. Daemen, A. J. Ramirez-Cuesta, M. Schröder, S. Yang, *Angew. Chem. Int. Ed. Engl.* **2022**, *61*, 202207259.
[10] Z. Han, J. Li, W. Lu, K. Wang, Y. Chen, X. Zhang, L. Lin, X. Han, S. J. Teat, M. D. Frogley, S. Yang, W. Shi, P. Cheng, *Angew. Chem. Int. Ed. Engl.* **2022**, *61*, 202115585.
[11] E. Martínez-Ahumada, D. W. Kim, M. Wahiduzzaman, P. Carmona-Monroy, A. López-Olvera, D. R. Williams, V. Martis, H. A. Lara-García, S. López-Morales, D. Solis-Ibarra, G. Maurin, I. A. Ibarra, C. S. Hong, *J. Mater. Chem. A* **2022**, *10*, 18636.
[12] E. Martínez-Ahumada, M. L. Díaz-Ramírez, H. A. Lara-García, D. R. Williams, V. Martis, V. Jancik, E. Lima, I. A. Ibarra, *J. Mater. Chem. A* **2020**, *8*, 11515.
[13] M. Savage, Y. Cheng, T. L. Easun, J. E. Eyley, S. P. Argent, M. R. Warren, W. Lewis, C. Murray, C. C. Tang, M. D. Frogley, G. Cinque, J. Sun, S. Rudić, R. T. Murden, M. J. Benham, A. N. Fitch, A. J. Blake, A. J. Ramirez-Cuesta, S. Yang, M. Schröder, *Adv. Mater.* **2016**, *28*, 8705.
[14] X. Cui, Q. Yang, L. Yang, R. Krishna, Z. Zhang, Z. Bao, H. Wu, Q. Ren, W. Zhou, B. Chen, H. Xing, *Adv. Mater.* **2017**, *29*, 1606929.
[15] P. Brandt, A. Nuhnen, M. Lange, J. Möllmer, O. Weingart, C. Janiak, *ACS Appl. Mater. Interfaces* **2019**, *11*, 17350.
[16] G. L. Smith, J. E. Eyley, X. Han, X. Zhang, J. Li, N. M. Jacques, H. G. W. Godfrey, S. P. Argent, L. J. McCormick McPherson, S. J. Teat, Y. Cheng, M. D. Frogley, G. Cinque, S. J. Day, C. C. Tang, T. L. Easun, S. Rudić, A. J. Ramirez-Cuesta, S. Yang, M. Schröder, *Nat. Mater.* **2019**, *18*, 1358.
[17] M. R. Tchalala, P. M. Bhatt, K. N. Chappanda, S. R. Tavares, K. Adil, Y. Belmabkhout, A. Shkurenko, A. Cadiau, N. Heymans, G. De Weireld, G. Maurin, K. N. Salama, M. Eddaodi, *Nat. Commun.* **2019**, *10*, 1328.
[18] L. M. Rodriguez-Albelo, E. Lopez-Maya, S. Hamad, A. R. Ruiz-Salvador, S. Calero, J. A. Navarro, *Nat. Commun.* **2017**, *8*, 14457.
[19] P. Brandt, S. H. Xing, J. Liang, G. Kurt, A. Nuhnen, O. Weingart, C. Janiak, *ACS Appl. Mater. Interfaces* **2021**, *13*, 29137.
[20] M. Woellner, S. Hausdorf, N. Klein, P. Mueller, M. W. Smith, S. Kaskel, *Adv. Mater.* **2018**, *30*, 1704679.
[21] L. S. Xie, G. Skorupskii, M. Dinca, *Chem. Rev.* **2020**, *120*, 8536.
[22] D. N. Dybtsev, H. Chun, K. Kim, *Angew. Chem., Int. Ed.* **2004**, *43*, 5033.
[23] S. Ehrling, I. Senkovska, V. Bon, J. D. Evans, P. Petkov, Y. Krupskaya, V. Kataev, T. Wulf, A. Krylov, A. Vtyurin, S. Krylova, S. Adichtchev, E. Slyusareva, M. S. Weiss, B. Büchner, T. Heine, S. Kaskel, *J. Mater. Chem. A* **2019**, *7*, 21459.
[24] X. Wang, Z. Niu, A. M. Al-Enizi, A. Nafady, Y. Wu, B. Aguila, G. Verma, L. Wojtas, Y.-S. Chen, Z. Li, S. Ma, *J. Mater. Chem. A* **2019**, *7*, 13585.
[25] S. Henke, W. Li, A. K. Cheetham, *Chem. Sci.* **2014**, *5*, 2392.
[26] D. Tanaka, S. Horike, S. Kitagawa, M. Ohba, M. Hasegawa, Y. Ozawa, K. Toriumi, *Chem. Commun.* **2007**, 3142.
[27] A. Nuhnen, C. Janiak, *Dalton Trans.* **2020**, *49*, 10295.
[28] P. M. Bhatt, Y. Belmabkhout, A. H. Assen, Ł. J. Weselinski, H. Jiang, A. Cadiau, D. X. Xue, M. Eddaoudi, *Chem. Eng. J.* **2017**, *324*, 392.
[29] S. H. Yang, J. L. Sun, A. J. Ramirez-Cuesta, S. K. Callear, W. I. F. David, D. P. Anderson, R. Newby, A. J. Blake, J. E. Parker, C. C. Tang, M. Schröder, *Nat. Chem.* **2012**, *4*, 887.
[30] D. Z. Zhang, J. F. Wu, P. Li, Y. H. Cao, *J. Mater. Chem. A* **2017**, *5*, 20666.
[31] H. Y. Xu, J. Z. Li, P. D. Li, J. J. Shi, X. W. Gao, W. B. Luo, *ACS Appl. Mater. Interfaces* **2021**, *13*, 49194.
[32] V. B. López-Cervantes, D. W. Kim, J. L. Obeso, E. Martínez-Ahumada, Y. A. Amador-Sánchez, E. Sánchez-González, C. Leyva, C. S. Hong, I. A. Ibarra, D. Solis-Ibarra, *Nanoscale* **2023**, *15*, 12471.
[33] N. Ingle, S. Mane, P. Sayyad, G. Bodkhe, T. Al-Gahouari, M. Mahadik, S. Shirsat, M. D. Shirsat, *Front. Mater.* **2020**, *7*, 93.
[34] N. Ingle, P. Sayyad, M. Deshmukh, G. Bodkhe, M. Mahadik, T. Al-Gahouari, S. Shirsat, M. D. Shirsat, *Appl. Phys. A* **2021**, *127*, 157.
[35] X. Zhang, Z. Zhai, J. Wang, X. Hao, Y. Sun, S. Yu, X. Lin, Y. Qin, C. Li, *ChemNanoMat* **2021**, *7*, 1117.
[36] Z. Zhai, X. Zhang, J. Wang, H. Li, Y. Sun, X. Hao, Y. Qin, B. Niu, C. Li, *Chem. Eng. J.* **2022**, *428*, 131720.
[37] Z. Zhai, J. Wang, Y. Sun, X. Hao, B. Niu, H. Xie, C. Li, *Appl. Surf. Sci.* **2023**, *613*, 155772.
[38] V. Chernikova, O. Yassine, O. Shekhah, M. Eddaoudi, K. N. Salama, *J. Mater. Chem. A* **2018**, *6*, 5550.
[39] M. E. DMello, N. G. Sundaram, A. Singh, A. K. Singh, S. B. Kalidindi, *Chem. Commun.* **2019**, *55*, 349.
[40] https://www.draeger.com/en_sea/Products/Pac-6000#related-product (accessed: January 2025).